Noise Analysis and Performance Improvement of a MEMS Fabry-Pérot Seismic Accelerometer

Minghui Zhao, Yonghong Qi, Xiaopeng Zhang, Bo Li, Zhuangde Jiang, and Xueyong Wei, *Senior Member, IEEE*

***Abstract*—MEMS accelerometers based on the optical interference technique play an important role in seismic wave detection due to their high resolution, strong electromagnetic stability, and low cost. This paper reports a MEMS Fabry-Pérot seismic accelerometer. The working principle and transfer function were established to introduce the accelerometer. Noise sources that contribute to the output of the accelerometer were analyzed and predicted. To improve the performance of the accelerometer, the active temperature compensation, the appropriate laser driving current selection, and the laser modulation-demodulation technologies were adopted to reduce the noise. Experimental results show that the noise floor of the accelerometer was decreased from 11 μg/$\sqrt{}$Hz@1 Hz to 330 ng/$\sqrt{}$Hz@1 Hz.**

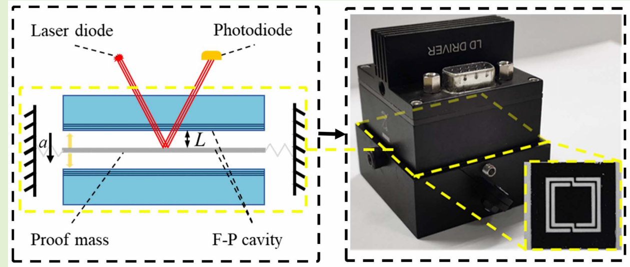

***Index Terms*—MEMS seismic accelerometer, Fabry-Pérot interference, noise equivalent acceleration.**

I. Introduction

SEISMOMETER is an instrument to accurately measure the seismic wave signals whether it is natural or artificial. Therefore, it is widely used in seismology, seismic exploration, and structural health monitoring [1]–[5]. Traditional commercial seismometer mainly includes torsion, pendulum, and force balance capacitive seismometer [6]–[8], whose resolution is ultrahigh. However, its volume is large, with price expensive. Attracted by the advantages of MEMS (Micro Electro Mechanical System) technology and the accuracy enhancement of the accelerometer, researchers begin developing the new MEMS seismic accelerometer [9]–[14].

Currently, the capacitive, resonant, electrochemical, and optical MEMS seismic accelerometers have been developed and reported [15]–[19]. Not only is their resolution the same as the traditional seismometers, but also the volume and cost are much lower, which show great application prospect. Among the above types, the optical MEMS seismic accelerometers based on the interference principle have a higher displacement detection accuracy (fm/$\sqrt{}$Hz level), lower thermal noise(thanks to the optical detection method is decoupled from the mechanical structure), and stronger anti-electromagnetic interference ability [20]. Although they own the above superiorities, it is still difficult to develop an optical seismic accelerometer with high resolution, as the optomechanical sensing structure, the light source, the photodetector, and the acquisition circuit all contribute to the noise of the accelerometer [21]. In the designing of the optomechanical sensing structure, the sensitivity, bandwidth, Brownian noise, and the fabricated process should be considered comprehensively, and the trade-off between them should be found. For the light source and photodetector, the laser driving, the temperature compensation, and the method of reducing optical noise should be paid special attention. Besides, suitable electronics components and signal processing methods should be adopted to establish a low noise acquisition circuit.

In this paper, we propose a MEMS Fabry-Pérot seismic accelerometer. The analytic model of the Fabry-Pérot interference and mass-spring system was established, and

Manuscript received October 9, 2021; accepted November 7, 2021. Date of publication November 16, 2021; date of current version December 29, 2021. This work was supported in part by the National Key Research and Development Program of China under Grant 2018YFB2002303, in part by the National Natural Science Foundation of China under Grant 52075432, in part by the Key Research and Development Program of Shaanxi Province under Grant 2018ZDCXL-GY-02-03, in part by the Program for Innovation Team of Shaanxi Province under Grant 2021TD-23, and in part by the International Joint Laboratory for Micro/Nano Manufacturing and Measurement Technologies. The associate editor coordinating the review of this article and approving it for publication was Prof. Sang-Seok Lee. *(Minghui Zhao and Yonghong Qi contributed equally to this work.) (Corresponding author: Xueyong Wei.)*

Minghui Zhao, Yonghong Qi, Bo Li, and Zhuangde Jiang are with the State Key Laboratory for Manufacturing Systems Engineering, Xi'an Jiaotong University, Xi'an 710049, China.

Xiaopeng Zhang is with the State Key Laboratory for Manufacturing Systems Engineering, Xi'an Jiaotong University, Xi'an 710049, China, and also with the Northwest Institute of Nuclear Technology, Xi'an 710024, China.

Xueyong Wei is with the State Key Laboratory for Manufacturing Systems Engineering, Xi'an Jiaotong University, Xi'an 710049, China, and also with the State Key Laboratory of Applied Optics, Changchun Institute of Optics, Fine Mechanics and Physics, Chinese Academy of Sciences, Changchun 130033, China (e-mail: seanwei@mail.xjtu.edu).

Digital Object Identifier 10.1109/JSEN.2021.3128534

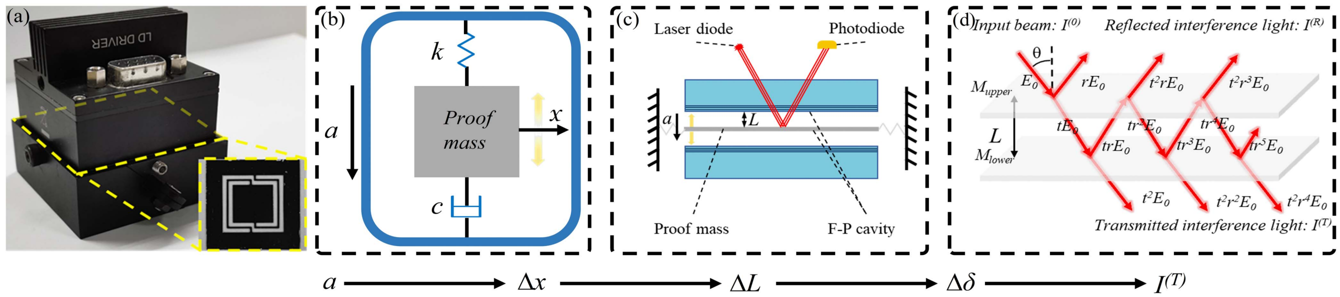

Fig. 1. (a) The package and the chip of the accelerometer (b) the equivalent mass-spring system of the accelerometer (c) Schematic diagram of the accelerometer (d) Fabry-Pérot interference with multiple rounds.

the transfer function from acceleration to light intensity was derived, and the influences of properties from the Fabry-Pérot cavity and mass-spring system on the performance of the accelerometer was analyzed. Then, the noise sources of the optical accelerometer were analyzed and predicted from mechanical, optical, and electrical aspects. Afterwards, the performance of two accelerometers with different geometric parameters was calibrated. Finally, the temperature compensation, the appropriate laser driving current selection, and the laser modulation-demodulation technology were utilized to reduce the noise of the accelerometer, and the experimental results show that the noise floor of the accelerometer is reduced by two orders of magnitude.

II. Working Principle

Fabry-Pérot interferometer was invented by Charles Fabry and Alfred Perot in 1897 [22], and it is widely used in spectrometers, filters, and sensors. In this paper, the Fabry-Pérot cavity was used as a sensitive component for an accelerometer by combining it with a mass-spring structure. The packaged accelerometer is shown in Fig.1(a), which is integrated with a laser diode, aspheric lens, photodiode, thermoelectric cooler (TEC), and MEMS sensor chip (zoomed inset of Fig.1(a)), which was fabricated by silicon wafer and bonded with BF33 glass, and the reflection coefficient of the mirror is 4%. The detail of the design and fabrication of the chip has been reported in the reference [9]. In this paper, we focus more on the noise analysis and suppression of the accelerometer.

The equivalent model of the accelerometer can be simplified as a second-order mass-spring system as shown in Fig. 1(b). The system consists of proof mass m, spring constant k and damping factor c. When the system is subjected to an acceleration a, the proof mass moves relative to the frame, the differential equation for the displacement x is obtained according to Newton's law [23]:

$$m\frac{d^2x(t)}{dt^2}+c\frac{dx(t)}{dt}+kx(t)=F_{ext}=ma(t) \tag{1}$$

where m is the weight of the proof mass, c is the damping coefficient, k is the spring constant, $x(t)$ is the displacement of the proof mass relative to the frame. Solving for x through Laplace transform yields the transfer function:

$$H=\frac{X(s)}{A(s)}=\frac{1}{s^2+s\frac{\omega_0}{Q}+\omega_0^2} \tag{2}$$

where $\omega_0=\sqrt{k/m}$ is the resonant frequency, $Q=\omega_0 m/c$ is the quality factor. The resonant frequency is a very important parameter that should be considered in the structure design because the displacement x is proportional to the acceleration a when the frequency of the acceleration is far below the resonant frequency, which determines the accelerometer's mechanical sensitivity. The sensitivity can be obtained according to Newton's second law and Hooke's law:

$$\begin{aligned} F &= ma = kx \\ S_M &= \frac{x}{a}=\frac{m}{k}=\frac{1}{\left(\sqrt{k/m}\right)^2}=\frac{1}{\omega_0^2}\left(m/m/s^2\right)=\frac{9.8}{\omega_0^2}\left(m/g\right) \end{aligned} \tag{3}$$

The subjected acceleration a makes the proof mass move, which changes the cavity length L of the Fabry-Pérot cavity as depicted in Fig. 1(c). The phase difference of the light which reflected off both mirrors of the Fabry-Pérot cavity also experiences a shift with the change of the cavity length L:

$$\Delta\delta=\left(\frac{2\pi}{\lambda}\right)2n\left(L_0+\Delta L\right)\cos\theta \tag{4}$$

where λ is the wavelength of the incident light in vacuum, n is the refractive index of the Fabry-Pérot cavity, L_0 is the initial cavity length, ΔL is the changes of the cavity length, and θ is the indecent angle of the light. Finally, the subjected acceleration a results in the change of the interference light intensity. Therefore, the interference light intensity under the subjected acceleration a can be expressed as:

$$\begin{aligned} I^{(T)} &= \frac{(1-R)^2}{1+R^2-2R\cos\delta}I^{(0)} \\ &= \frac{(1-R)^2}{1+R^2-2R\cos\left(\frac{4\pi n}{\lambda\omega_0^2}a+\frac{4\pi nL_0}{\lambda}\right)}I^{(0)} \end{aligned} \tag{5}$$

The normalized intensity versus the subjected acceleration is simulated by Matlab whose results are shown in Fig.2. It can be obtained that the higher reflectivity of the cavity, the narrower the transmission peak, and the higher sensitivity of the accelerometer.

Besides, Fig.2 shows that the slope has a maximum value as the points indicated, which corresponds to the maximum optical sensitivity of the accelerometer, and it can be expressed as:

$$S_O=\frac{I^{(0)}\pi}{\lambda}\sqrt{F-1}\left(W/m\right) \tag{6}$$

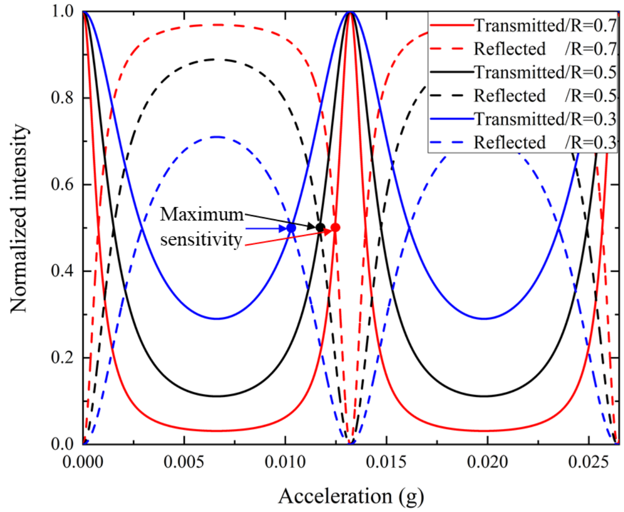

Fig. 2. Simulation of the normalized intensity versus the acceleration.

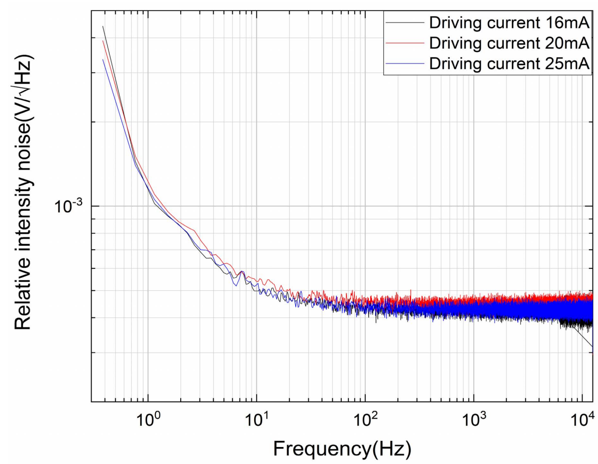

Fig. 3. The RIN of the adopted laser diode with the different driving currents.

where $F = 4R/(1-R)^2$ is the fineness of the Fabry-Pérot cavity, which is determined by the reflectance of the two mirrors. Therefore, the total sensitivity of the MEMS Fabry-Pérot accelerometer is calculated as:

$$S_{total} = S_O S_M G_A = \frac{I^{(0)}\pi g}{\lambda \omega_0^2}\sqrt{F-1}\,(A/g) \tag{7}$$

where G_A is the responsivity of the photodiode(Thorlabs FDS100: 0.65A/W).

III. Performance Calibration and Noise Analysis

A. Noise Analysis

For the proposed accelerometer, the MEMS structure, optical detection method, and signal processing technology all contribute to the noise of the accelerometer output. Specifically, the total noise of the accelerometer consists of Brownian noise, laser relative intensity noise (RIN), photodiode shot and dark current noise, and transimpedance amplifier noise. Therefore, the total noise equivalent acceleration (NEA) is the summation of the acceleration spectral density (ASD) of the noise sources:

$$NEA_{total} = \sqrt{NEA_{Brown}^2 + NEA_{RIN}^2 + NEA_{pd}^2 + NEA_{trans}^2} \tag{8}$$

NEA_{Brown} due to the thermal agitation of the air molecules around the micromachined proof mass[24] is expressed by:

$$NEA_{Brown} = \sqrt{\frac{4k_B T_{ambient}\omega_0}{mQ}} \tag{9}$$

where k_B is the Boltzmann constant, $T_{ambient}$ is the ambient temperature, m is the weight of the proof mass, ω_0 is the resonant frequency of the mass-spring structure, Q is the mechanical quality factor. Since the NEA_{Brown} is determined by the mechanical structure of the accelerometer. Eq.(9) can be rewritten in the form directly related to structural parameters:

$$NEA_{Brown} = \sqrt{\frac{4k_B T_{ambient}\omega_0}{mQ}} = \sqrt{\frac{4k_B T_{ambient}c}{m^2}} = \sqrt{\frac{4k_B T_{ambient}\frac{\mu L^4}{h^3}\beta}{(\rho L^2 H)^2}} = \sqrt{\frac{4k_B T_{ambient}\mu\beta}{(\rho H)^2 h^3}} \tag{10}$$

where μ is the viscosity of gas, β is the coefficient of damping force, ρ is the density of silicon, H is the thickness of the proof mass, and h is the gap from the mass to the fixed mirror. Eq.(10) indicates that NEA_{Brown} is related to H, h, *and* μ, so we can reduce NEA_{Brown} by increasing the cavity length or change the vacuum.

RIN is one of the intrinsic noises of the laser diode because of the random intensity fluctuations of the semiconductor laser output [28]. RIN distribution with frequency of the adopted laser diode (Thorlabs HL6748MG) was tested and recorded in Fig.3. Results show that the RIN in 1 Hz is approximate 6×10^{-4} V/$\sqrt{}$Hz, and RIN is higher in frequency before 100 Hz, which is due to the existence of the 1/f and G-R (generation-recombination) noise. While the RIN is lower in frequency after 100 Hz and appears as white noise which corresponds to the thermal and shot noise of semiconductor laser diode.

The accelerometer in this paper is used for seismic wave detection, whose bandwidth is from 0.1 Hz to100 Hz, it is necessary to reduce the RIN of the laser diode at frequencies below 100 Hz. The laser modulation- demodulation technologies and reference detection circuit operation are often applied. The former can be directly realized by laser modulation and cross-correlation signal detection, while the latter needs to implement an additional reference diode that is more complicated. Therefore, the laser modulation demodulation technology will be applied to suppress RIN of the laser source.

The shot noise and dark current noise from the photodiode are determined by the photocurrent collected by the photodiode and dark current of the photodiode, which is calculated

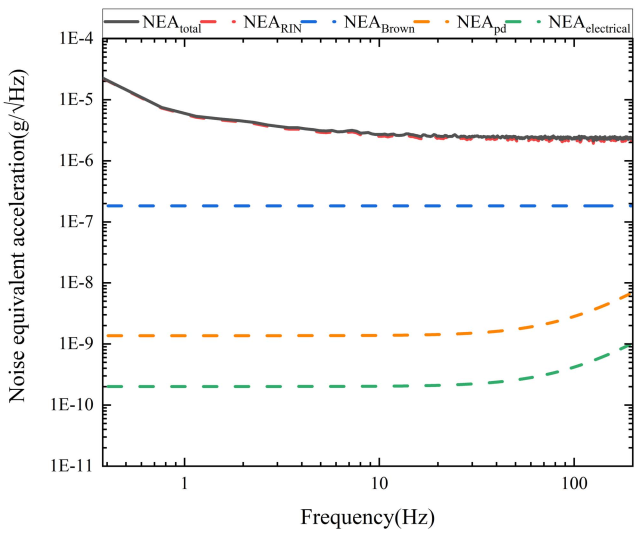

Fig. 4. Predicted NEA contribution from each of the noise sources.

as:

$$NEA_{pd} = \frac{\sqrt{2ei_{pd}}}{S_{total}} \tag{11}$$

where e is the charge of an electron, i_{pd} is the current generated in the photodiode and dark current of the photodiode, S_{total} is the sensitivity of the accelerometer. For our accelerometer, the current generated in the photodiode is 520 μA, and the dark current of the adapted photodiode (Thorlabs FDS100) is 1 nA~20nA.

After the interference light is collected by the photodiode. The photocurrent should be converted to voltage by a transimpedance amplifier, which inevitably introduces the electrical noise in the process. In this paper, a commercial low-noise current preamplifier (Stanford Research Systems SR570) was used to convert and amplify the current. The current noise of the transimpedance amplifier (N_{trans}) under the gain condition (1 mA/V) is 150 pA/$\sqrt{}$Hz. The transimpedance noise is equivalent to acceleration by:

$$NEA_{trans} = \frac{N_{trans}}{S_{total}} \tag{12}$$

Under the above analysis, the noise sources are predicted and shown in Fig.4. The total noise equivalent acceleration of the accelerometer is close to 3.5 μg/$\sqrt{}$Hz. Brownian noise appears as white noise, while other noise sources are dependent on frequency. Besides, it can be found that the RIN is the main noise source, and the RIN is much lower in the high-frequency band.

B. Performance Calibration

To calibrate the performance of the accelerometer, a static gravity rotation test was performed as shown in Fig.5. In this experiment, a constant current laser driver was utilized to drive the laser, and the value of 20 mA was selected. The accelerometer was mounted on the precision rotation stage, thus the component of gravity g$*$sinθ was applied to the sensor chip along the sensing direction of the accelerometer, and it can be changed by turning the rotation stage with a certain angle θ. Finally, the light with the information of the gravity was collected by the photodiode and recorded in the Digit Multimeter (KEYSIGHT 34470A).

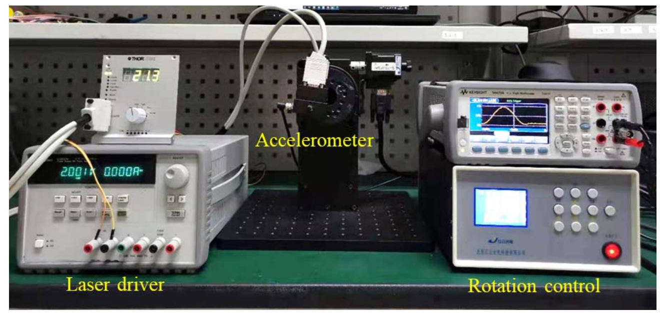

Fig. 5. The calibration setup for the static gravity measurement.

During this test, the rotation stage was accurately controlled to revolve with a step of 0.05°, and the output of the accelerometer was changed with the rotation of the stage as displayed in the Digit Multimeter. More data were depicted in Fig.6(a), which shows the output of two different accelerometers with different sensitivities. The output of the accelerometer periodically changes with the rotation of the stage which is consistent with Eq.(5) and Fig.2.

It also can be seen that there exist the phase and period differences of accelerometers 1 and 2. The phase of the accelerometer's output is $4\pi nL_0/\lambda$ which is determined by the initial cavity length of the Fabry-Pérot cavity as equation (5) described. Because of the fabrication and assemble errors, the initial cavity lengths of accelerometers 1 and 2 are different, which result in the phases of accelerometers 1 and 2 are different. The period of the accelerometer's output can be obtained from equation (5), it is mainly determined by the cosine term, the period is deduced to be $\lambda\omega_0^2/2n$. Thus, the periods of accelerometers 1 and 2 are different because of the difference of ω_0.

A section of the data in the red dash box marked in Fig.6(a) was extracted to show the output of the accelerometer accurately and linearly fitted to calculate the sensitivity. Results were shown in Fig.6(b) which indicated that the sensitivity of the two accelerometers was 50.173 and 7.301 V/g respectively. The sensitivity of accelerometer 2 is much bigger than accelerometer 1. It is because the spring beam of accelerometer 2 is thinner than accelerometer 1, resulting in a smaller resonant frequency. The smaller the resonant frequency, the bigger the sensitivity.

Next, the static output of the accelerometers was sampled with a frequency of 25 Hz, the results of which were recorded in Fig.6(c). The voltage spectral density of the output voltage in Fig.6(c) was calculated [30], which was transformed into acceleration combined with the obtained sensitivity as showed in Fig.6(d). The output ASD (Acceleration Spectral Density) of the two accelerometers is 35 and 11 μg/$\sqrt{}$Hz@0.1Hz respectively. It can be found that the output ASD is close to equal at frequencies greater than 0.5 Hz. It is because that the higher the sensitivity of the accelerometer, the easier it is to be influenced by ambient vibration. The analysis above also can be proved from the zoomed inset of Fig.6(c), where it is

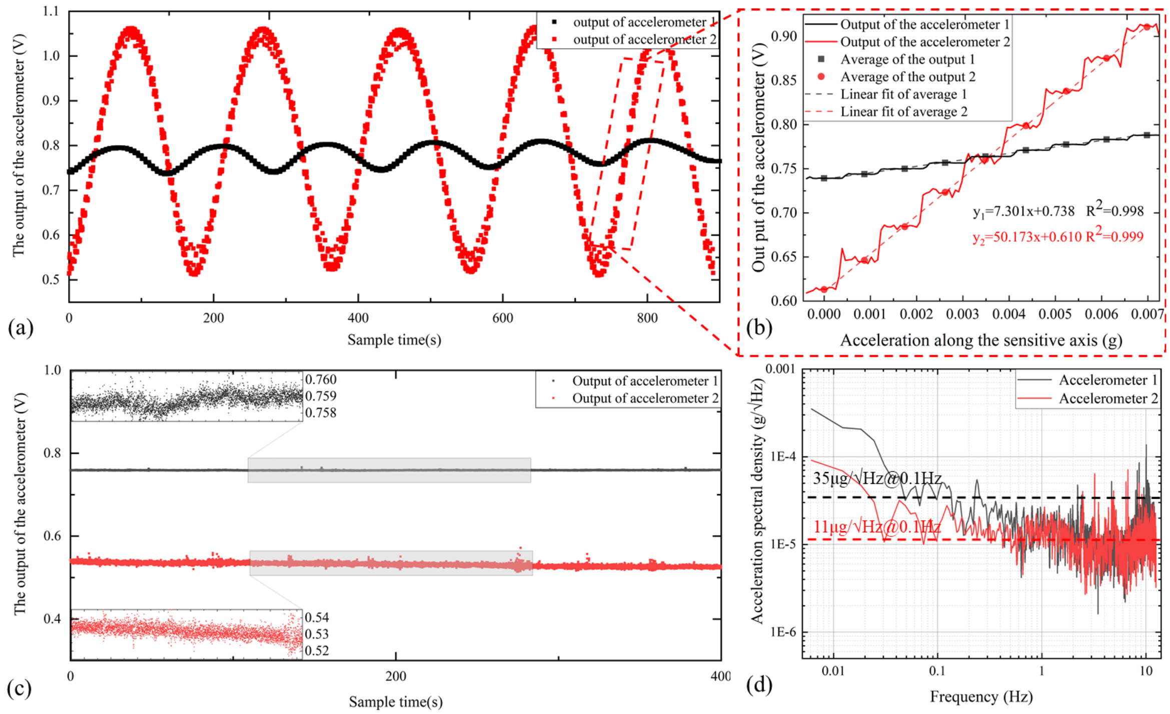

Fig. 6. The calibration results of two accelerometers with different structure parameters (a) output of the accelerometer with the rotation of the stage (b) sensitivity of the accelerometer (c) static output of the accelerometer (d) the ASD of the accelerometer.

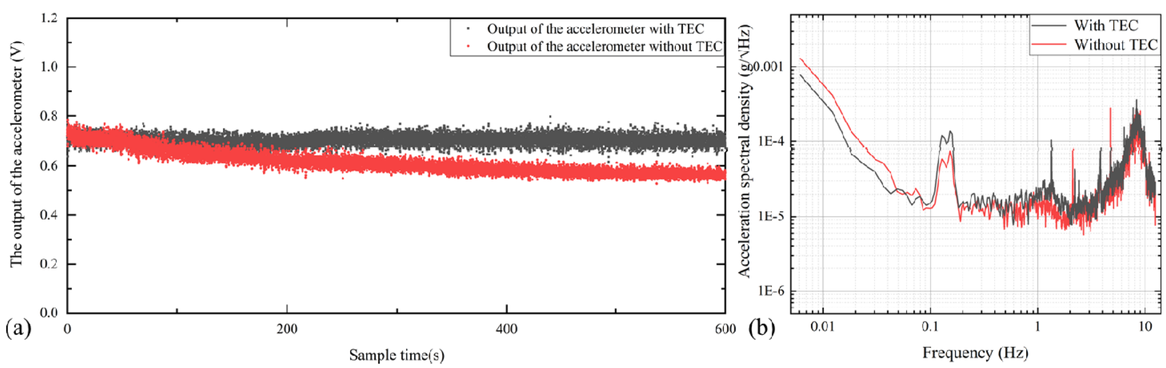

Fig. 7. The comparison between the output of the accelerometer with and without TEC (a) static output (b) the ASD of the accelerometer.

clear that the fluctuation of accelerometer 2 is 10 times bigger than accelerometer 1.

IV. Performance Improvement

The noise analysis and performance calibration of the seismic accelerometer was performed in Section III. The results show that the noise level of the accelerometer is higher than the earth's background ground noise (new high noise model, NHNM). In this section, different methods were adopted to improve the performance of the accelerometer, and all studies were performed with accelerometer 2 calibrated in Section III.

A. Temperature Compensation

Laser diode is sensitive to temperature fluctuations which can affect the performance of the reported accelerometer. Therefore, the temperature compensation was performed to make up for these disadvantages. The method is to establish a proportion integration differentiation (PID) temperature control system which consists of a thermistor and a TEC. The thermistor was applied to measure the temperature of the laser diode, and the TEC was used to heat or cool the laser diode under the measured results from the thermistor, and the process is controlled by the PID algorithm.

To evaluate the effects of the adopted temperature compensation system, the output of the accelerometer with and without TEC was collected and recorded in Fig.7(a), in which the output of the accelerometer without TEC decreases, because the temperature of the laser diode increases with the working times accumulating, and the output power of the laser diode decreases with the increasing of the temperature. While it is obvious that the output of the accelerometer with TEC is relatively stable. The ASD of the accelerometer with and without TEC was calculated and depicted in Fig.7(b). Results show that the ASD of the accelerometer with TEC is a little higher than without TEC, owing to the continuously adjusted temperature by the PID temperature control system which results in the fluctuations of the laser output. Although the ASD of the accelerometer with TEC is worse than without

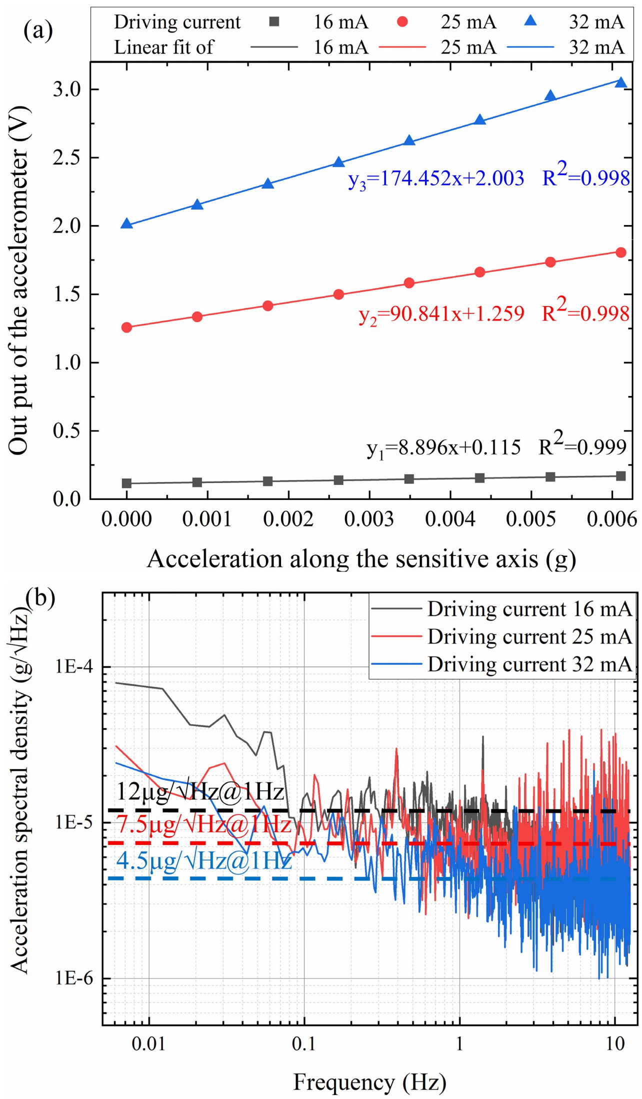

Fig. 8. The calibration results of the accelerometer with different driving current (a) sensitivity (b) noise equivalent acceleration.

TEC, its long-term stability is better and it can protect the laser diode from damaged.

B. Laser Driving Current Selection

Laser driving current is one of the most important parameters of the laser diode, which decides the output power, stability, and lifetime of the laser diode. The commercial laser diode whose datasheet always provides the threshold, operating, and maximum current. Thus, it is difficult to select the suitable one to drive the laser diode of the accelerometer. The current lower than the threshold is more stable because the laser diode generates very little heat, while its output power is small. The current is equal to the operating current with high output power but low temperature stability. The current higher than the threshold but lower than the operating current whose output power and temperature stability are somewhere between the above two stated.

For the reported accelerometer, the resolution and sensitivity are the most important parameters. Therefore, they are used as the assessment standard to choose suitable driving current.

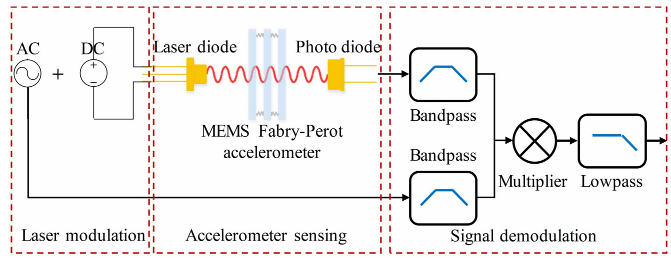

Fig. 9. The laser modulation-demodulation technology of the reported accelerometer.

Next, the current 16 mA, 25mA, 32mA was adopted to drive the laser diode. The sensitivity and ASD test were performed whose method is the same as the one used in section III.B. The results are shown in Fig.8, which indicate that the higher the driving current we used, the higher sensitivity and lower noise equivalent acceleration are. The reason is the sensitivity increases linearly with laser intensity while shot noise is proportional to the square root of the intensity. Therefore, better performance of sensitivity and resolution can be obtained when adopting a higher driving current. More specifically, the acceleration noise corresponding to the shot noise is reduced by selecting a higher driving current [31].

C. Laser Modulation-Demodulation Technology

The RIN is the main noise for the accelerometer in this paper, and it decreases with the frequency increasing as tested in section III. A. Therefore, we use laser modulation demodulation technology (as depicted in Fig.9) to reduce the RIN. This technology includes two processes of modulation and demodulation. The seismic signal to be measured is always at low-frequency band, while the RIN of the laser diode is at the same frequency band. Therefore, in the laser modulation, the laser diode is modulated to operate at high frequency to reduce the influence of 1/f component from RIN. This process also shifts the measured signal to the high frequency band. To revert the measured signal, the demodulation technology based on the cross-correlation principle is adopted. The modulated signal is regular, but the noise signal is random, so the signal and the noise are not correlated. We construct a reference signal with the same frequency as the modulated frequency, and multiply it with the modulated signal. Then the phase information and noise signal of the input signal are filtered through the FIR low-pass filter. Finally, there just remains the amplitude information of the signal to be measured.

For the reported seismic accelerometer, the frequency of the seismic wave to be measured is 0.1-20 Hz, which determines the parameters of the filters. In Fig.9, the center frequency of the bandpass filter is 10 kHz which is the same as the modulation frequency, and the bandwidth of the filter is 5 kHz, it could let the modulated seismic signal pass, but filter the noise out of the frequency band. The cutoff frequency of the lowpass filter is set as 25 Hz which could filter the noise without affect the seismic signal.

During the operation, a DC(30mA) combined with a sinusoidal AC (amplitude:8 mA, frequency:10 kHz) current was used to drive the laser diode, then the light incident to the

TABLE I

COMPARISON BETWEEN THE FABRY-PÉROT ACCELEROMETER REPORTED FROM 1998 TO 2021

Reference	[32]	[33]	[34]	[35]	[36]	[37]	[38]
Year	1998	2006	2010	2011	2012	2013	2014
Type	Fiber MEMS	Fiber MEMS	Fiber Mechanical	All Fiber	Fiber MEMS	Fiber Mechanical	All Fiber
Noise/Resolution	1mg	2.9μg	842ng	20μg	111μg	450μg/√Hz	835ng

[39]	[40]	[41]	[42]	[43]	[44]	[45]	[46]	This work
2014	2017	2017	2018	2018	2019	2020	2021	2021
Fiber MEMS	All Fiber	All Fiber	All Fiber	Fiber MEMS	Fiber MEMS	Fiber MEMS	Fiber MEMS	Integrated Optical
60μg/√Hz	20μg/√Hz	10mg	5μg/√Hz	31.2μg/√Hz	4.12μg/√Hz	100ng/√Hz	309μg	330ng/√Hz

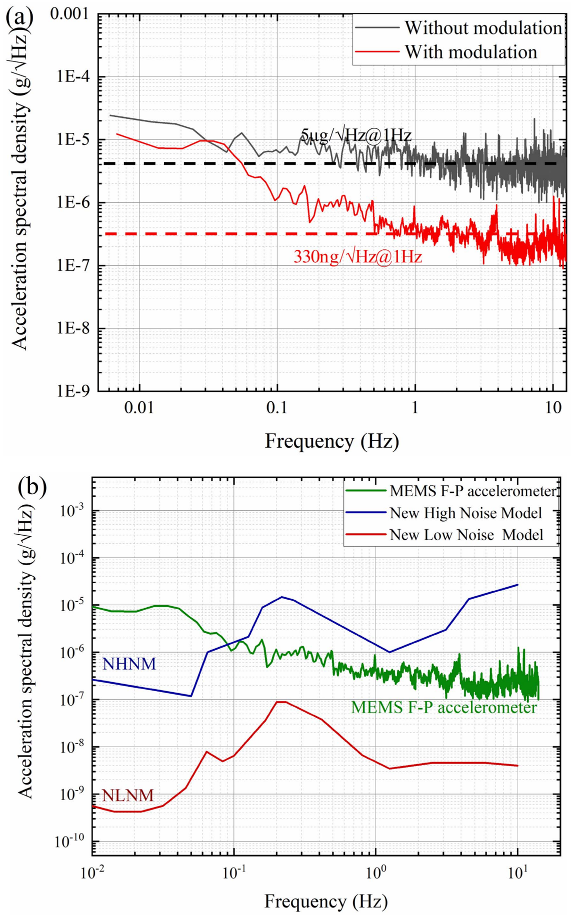

Fig. 10. (a) The measured ASD of the accelerometer with and without modulation (b) the ASD contrast between the accelerometer and the NHNM, NLNM.

accelerometer was collected by the photodiode. The photocurrent was transformed to voltage through a transimpedance amplifier (TIA). The voltage signal was sent to a band-pass filter to reduce low frequency noise because the light was modulated to high frequency. Finally, the signal was multiplied with the modulation AC voltage, and pass through a low pass filter to revert the signal with useful information. As above stated, the ASD of the accelerometer with and without modulation is measured and depicted in Fig.10(a). Results show that the ASD with modulation is 330 ng/$\sqrt{}$Hz@1Hz which is smaller than that without modulation (5 μg/$\sqrt{}$Hz@1Hz). The ASD contrast between the accelerometer and the earth noise model is shown in Fig.10(b) which indicates the noise floor of the reported accelerometer is lower than the earth's background noise (the new high noise model, NHNM) at frequency after 0.1 Hz. Therefore, the accelerometer can be used as a short-period seismometer.

For comparison, the noise/resolution of the Fabry-Pérot accelerometers was listed in Tab.I from 1998 to 2021. In Tab.I, there are four types of Fabry-Pérot accelerometer, they are fiber MEMS, fiber mechanical, all fiber, and integrated optical, respectively. It's obvious that the reported accelerometer in this paper with superior noise floor than other accelerometers except reference [45]. Besides, unlike other reported work, the integrated optical Fabry-Pérot accelerometer was developed in a small package with a size of 50 mm×50 mm×50 mm, which is more stable and portable to be used outdoors.

V. CONCLUSION

In conclusion, a MEMS Fabry-Pérot seismic accelerometer was reported. The working principle and the transfer function of the accelerometer were introduced and derived after the establishment of the Fabry-Pérot interference and mass-spring models, from which the reflectance of the mirror and the resonant frequency of the mass-spring structure are the key parameters for the accelerometer designing can be obtained. Afterwards, the noises originate from optical, mechanical, and electrical aspects were analyzed and the NEA was theoretically predicted, which implies RIN is the main noise source. The total noise equivalent acceleration is close to 3.5 μg/$\sqrt{}$Hz. Then, the performance of two accelerometers with different resonant frequencies (due to the difference of spring beam thickness) was calibrated. Results show that the sensitivity of the two accelerometers was 50.173 V/g and 7.301 V/g respectively. The ASD of the two accelerometers was also tested, the value is 35 and 11 μg/$\sqrt{}$Hz@0.1 Hz respectively, which is close to the total NEA as analyzed in section III. Finally, to degrade the noise of the accelerometer, the active temperature compensation methods with TEC, the laser driving current selection, and the laser modulation-demodulation technology were used, the experiment results show that the ASD of the accelerometer is reduced from 11 μg/$\sqrt{}$Hz@1 Hz to 330 ng/$\sqrt{}$Hz@1 Hz, which suggest that the reported MEMS Fabry-Pérot seismic accelerometer has a good potential in seismic wave detection.

REFERENCES

[1] J. Havskov and G. Alguacil, *Instrumentation in Earthquake Seismology*. New York, NY, USA: Springer, 2010, pp. 5–7.

[2] P.-L. Huang, T.-L. Lin, H.-J. Hsiao, and R.-H. Huang, "Taiwan borehole seismometer application in earthquake early warning," *Terr., Atmos. Ocean. Sci.*, vol. 27, no. 6, pp. 819–824, 2016.

[3] R. Zachariadis, H. Thomason, and H. Teague, "Ocean bottom seismometers in seismic exploration surveys: Planning and operations," *Seg Tech. Program. Expanded Abstr.*, vol. 2, no. 1, pp. 651–652, 1983.

[4] R.-C. Yin, Y.-M. Wu, and T.-Y. Hsu, "Application of the low-cost MEMS-type seismometer for structural health monitoring: A pre-study," in *Proc. IEEE Int. Instrum. Meas. Technol. Conf. Proc.*, May 2016, pp. 1–5.

[5] J. Laine and D. Mougenot, "Benefits of MEMS based seismic accelerometers for oil exploration," in *Proc. Int. Solid-State Sensors, Actuat. Microsyst. Conf.*, 2007, pp. 10–14.

[6] J. A. Anderson and H. O. Wood, "Description and theory of the torsion seismometer," *Bull. Seismol. Soc. Amer.*, vol. 15, no. 1, pp. 71–72, 1925.

[7] J. Milne, "Pendulum seismometers," *Nature*, vol. 37, no. 963, pp. 570–571, Apr. 1888.

[8] I. P. Bashilov, S. G, Volosov, Y. N. Zubko, and S. A. Korolyov, "Portable digital seismometer," *Seismic Instrum.*, vol. 47, no. 1, pp. 80–88, Jan. 2011.

[9] M. Zhao, K. Jiang, H. Bai, H. Wang, and X. Wei, "A MEMS based Fabry–Pérot accelerometer with high resolution," *Microsyst. Technol.*, vol. 26, no. 6, pp. 1961–1969, Jan. 2020.

[10] S. Tang *et al.*, "A high-sensitivity MEMS gravimeter with a large dynamic range," *Microsyst. Nanoeng.*, vol. 5, no. 1, pp. 1–11, Oct. 2019.

[11] L. Xu, S. Wang, Z. Jiang, and X. Wei, "Programmable synchronization enhanced MEMS resonant accelerometer," *Microsyst. Nanoeng.*, vol. 6, no. 1, p. 63, Dec. 2020.

[12] A. Holland, "Earthquake data recorded by the MEMS accelerometer," *Seismol. Res. Lett.*, vol. 74, no. 1, pp. 20–26, Feb. 2003.

[13] G. Alguacil and J. Havskov, "Seismic accelerometers," in *Encyclopedia of Earthquake Engineering*, M. Beer, I. A. Kougioumtzoglou, E. Patelli, and S.-K. Au, Eds. Berlin, Germany: Springer, 2015, pp. 2504–2519, doi: 10.1007/978-3-642-35344-4.

[14] D. Mougenot and N. Thorburn, "MEMS-based 3D accelerometers for land seismic acquisition: Is it time?" *Lead. Edge*, vol. 23, no. 3, pp. 246–250, Mar. 2004.

[15] W. T. Pike, I. M. Standley, S. B. Calcutt, and A. G. Mukherjee, "A broad-band silicon microseismometer with 0.25 NG/rtHz performance," in *Proc. IEEE Micro Electro Mech. Syst. (MEMS)*, Belfast, U.K., 2018, pp. 113–116.

[16] X. Zou, P. Thiruvenkatanathan, and A. A. Seshia, "A seismic-grade resonant MEMS accelerometer," *J. Microelectromech. Syst.*, vol. 23, no. 4, pp. 768–770, Aug. 2014.

[17] T. Deng, D. Chen, J. Chen, Z. Sun, G. Li, and J. Wang, "Microelectromechanical systems-based electrochemical seismic sensors with insulating spacers integrated electrodes for planetary exploration," *IEEE Sensors J.*, vol. 16, no. 3, pp. 650–653, Feb. 2016.

[18] T. Chang *et al.*, "Fiber optic interferometric seismometer with phase feedback control," *Opt. Exp.*, vol. 28, no. 5, pp. 6102–6122, 2020.

[19] D. J. Milligan, B. Homeijer, and R. Walmsley, "An ultra-low noise MEMS accelerometer for seismic imaging," in *Proc. IEEE Sensors*, Oct. 2011, pp. 1281–1284.

[20] D. W. Carr, G. R. Bogart, S. Goodman, P. Baldwin, and D. Robinson, "A laser interferometric miniature seismometer," Monit. Res. Rev., Ground Based Nucl. Explosion Monit. Technol., Portsmouth, U.K., Tech. Rep. DE-FG02-08ER85108, Sep. 2008.

[21] M. S. Fralick, "Noise compensation and bias stability improvement methods for a micro-optical-electrical-mechanical accelerometer," M.S. thesis, Dept. Elect. Comput. Eng., San Diego State Univ., San Diego, CA, USA, 2012.

[22] C. Fabry and A. Perot, "Sur les franges des lames minces argentées et leur application à la mesure de petites épaisseurs d'air," *Ann. Chim. Phys.*, vol. 12, pp. 459–501, Dec. 1897.

[23] B. Boser and R. Howe, "Surface micromachined accelerometers," *IEEE J. Solid-State Circuits*, vol. 31, no. 3, pp. 366–375, Mar. 1996.

[24] H.-L. Chau and K. D. Wise, "Noise due to Brownian motion in ultrasensitive solid-state pressure sensors," *IEEE Trans. Electron Devices*, vol. ED-34, no. 4, pp. 859–865, Apr. 1987.

[25] N. A. Hall *et al.*, "Micromachined accelerometers with optical interferometric read-out and integrated electrostatic actuation," *J. Microelectromech. Syst.*, vol. 17, no. 1, pp. 37–44, Feb. 2008.

[26] S. Gao *et al.*, "High-resolution micro-grating accelerometer based on a gram-scale proof mass," *Opt. Exp.*, vol. 27, no. 23, pp. 34298–34311, Nov. 2019.

[27] N. C. Loh and M. A. Schmidt, "Sub-10 cm^3 interferometric accelerometer with nano-g resolution," *J. Microelectromech. Syst.*, vol. 11, no. 3, pp. 182–187, Jun. 2002.

[28] R. H. Olsson, B. E. N. Keeler, D. A. Czaplewski, and D. W. Carr, "Circuit techniques for reducing low frequency noise in optical MEMS position and inertial sensors," in *Proc. IEEE Int. Symp. Circuits Syst.*, New Orleans, LA, USA, May 2007, pp. 2391–2394.

[29] M. Rakhmanov, "Demodulation of intensity and shot noise in the optical heterodyne detection of laser interferometers for gravitational waves," *Appl. Opt.*, vol. 40, no. 36, pp. 6596–6605, Dec. 2001.

[30] A. D'Alessandro, G. Vitale, S. Scudero, R. D'Anna, and L. Greco, "Characterization of MEMS accelerometer self-noise by means of PSD and Allan Variance analysis," in *Proc. IEEE Int. Workshop Adv. Sensors Interface*, Vieste, Italy, Dec. 2017, pp. 159–164.

[31] R. Littrell, N. A. Hall, M. Okandan, R. Olsson, and D. Serkland, "Impact of relative intensity noise of vertical-cavity surface-emitting lasers on optics-based micromachined audio and seismic sensors," *Appl. Opt.*, vol. 46, no. 28, pp. 6907–6911, Sep. 2007.

[32] G. Schröpfer, W. Elflein, M. de Labachelerie, H. Porte, and S. Ballandras, "Lateral optical accelerometer micromachined in (100) silicon with remote readout based on coherence modulation," *Sens. Actuators A, Phys.*, vol. 68, nos. 1–3, pp. 344–349, Jun. 1998.

[33] M. Perez and A. A. Shkel, "Performance trade-offs of an interferometric micro-G resolution accelerometer," in *Proc. IEEE Sensors*, Daegu, South Korea, Oct. 2006, pp. 1357–1360.

[34] T. Ke, T. Zhu, Y. Rao, and M. Deng, "Accelerometer based on all-fiber Fabry–Pérot interferometer formed by hollow-core photonic crystal fiber," *Microw. Opt. Technol. Lett.*, vol. 52, no. 11, pp. 2531–2535, Nov. 2010.

[35] Z. Ran, E. Lu, Y. Rao, M. Ni, F. Peng, and D. Zeng, "Fiber-optic Fabry–Perot interferometer tip accelerometer fabricated by laser-micromachining," in *Proc. 21st Int. Conf. Opt. Fiber Sensors*, Ottawa, CA, Canada, May 2011, pp. 1–5.

[36] K. Zandi, J. A. Belanger, and Y.-A. Peter, "Design and demonstration of an in-plane silicon-on-insulator optical MEMS Fabry–Pérot-based accelerometer integrated with channel waveguides," *J. Microelectromech. Syst.*, vol. 21, no. 6, pp. 1464–1470, Dec. 2012.

[37] D. H. Wang and P. G. Jia, "Fiber optic extrinsic Fabry–Perot accelerometer using laser emission frequency modulated phase generated carrier demodulation scheme," *Opt. Eng.*, vol. 52, no. 5, May 2013, Art. no. 055004.

[38] Q. Zhang *et al.*, "All-fiber vibration sensor based on a Fabry–Perot interferometer and a microstructure beam," *J. Opt. Soc. Amer. B, Opt. Phys.*, vol. 30, no. 5, pp. 1211–1215, May 2013.

[39] E. Davies, D. S. George, and A. S. Holmes, "Remote photothermal actuation for calibration of in-phase and quadrature readout in a mechanically amplified Fabry–Pérot accelerometer," *IEEE Photon. J.*, vol. 6, no. 3, pp. 1–15, Jun. 2014.

[40] J. Cheng, X. Wu, S. Li, Q. Ge, D. Guang, and B. Yu, "A novel and miniaturized FPI accelerometer based on a spherical air cavity at fiber end," in *Proc. Int. Conf. Opt. Instrum. Technol., Adv. Opt. Sensors Appl.*, Beijing, China, Jan. 2018, pp. 1–6.

[41] J. Li *et al.*, "Micro-machined optical fiber side-cantilevers for acceleration measurement," *IEEE Photon. Technol. Lett.*, vol. 29, no. 21, pp. 1836–1839, Nov. 1, 2017.

[42] B. Liu *et al.*, "Extrinsic Fabry–Perot cantilever accelerometer based on micromachined 45° angled fiber," *J. Lightw. Technol.*, vol. 36, no. 11, pp. 2196–2203, Jun. 1, 2018.

[43] F. Y. Wang *et al.*, "All-optical accelerometer based on micromachined silicon wafer," in *Proc. Fiber Optic Sens. Opt. Commun.*, Beijing, China, 2018, pp. 1–6.

[44] S. Li, X. Wu, J. Shi, Q. Ge, G. Zhang, and B. Yu, "Fabry–Perot interferometer based on an aluminum-polyimide composite diaphragm integrated with mass for acceleration sensing," *IEEE Access*, vol. 7, pp. 186510–186516, 2019.

[45] Z. Q. Qu *et al.*, "A high-sensitivity optical MEMS accelerometer based on SOI double-side micromachining," in *Proc. IEEE Sensors*, Rotterdam, The Netherlands, Dec. 2020, pp. 1–4.

[46] M. Taghavi, H. Latifi, G. M. Parsanasab, A. Abedi, H. Nikbakht, and M. H. Poorghadiri, "A dual-axis MOEMS accelerometer," *IEEE Sensors J.*, vol. 21, no. 12, pp. 13156–13164, Jun. 2021.